Fabrication of high-frequency microfluidic oscillators with integrated thermal instrumentation

Georges Saliba, Thierry Camps, Vincent Raimbault, Lucien Baldas

Graphical Abstract

Fabrication of high-frequency microfluidic oscillators with integrated thermal instrumentation

Georges Saliba, Thierry Camps, Vincent Raimbault, Lucien Baldas

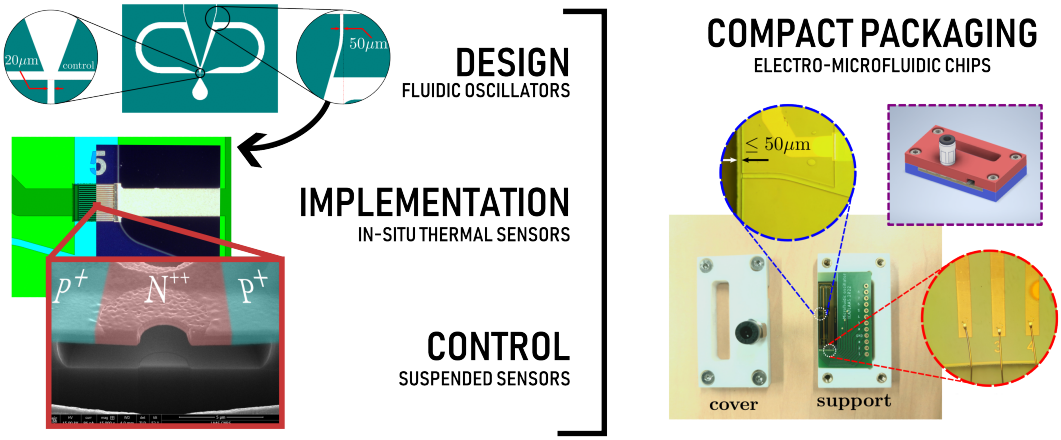

Highlights

Fabrication of high-frequency microfluidic oscillators with integrated thermal instrumentation

Georges Saliba, Thierry Camps, Vincent Raimbault, Lucien Baldas

- Fabrication of suspended, highly sensitive, rapid, non invasive thermal sensors embedded in microfluidic oscillators having a critical dimension of 20µm and with gas as working fluid.
- The electro-microfluidic chip enables the study of supersonic jet switching at high frequencies inside the oscillator.

Fabrication of high-frequency microfluidic oscillators with integrated thermal instrumentation

Georges Saliba[a], Thierry Camps[b], Vincent Raimbault[b], Lucien Baldas[a]

[a] *Institut Clément Ader (ICA), Université de Toulouse, CNRS, INSA, ISAE-SUPAERO, Mines-Albi, UPS, Toulouse, 31400, France*
[b] *CNRS, LAAS, 7 Avenue du Colonel Roche, Toulouse, F-31400, France*

Abstract

Fluidic devices were once a staple of control systems in harsh environments such as nuclear power plants or satellites, until they were superseded by electronic systems whose performance and size were rapidly improving. Nevertheless, the simplicity, robustness and autonomy of fluidic devices remain attractive features in many fluids engineering applications. In this study, a microfluidic oscillator, with a main jet only 20 microns wide, is produced, instrumented and tested. Particular to this study is the use of temperature micro-sensors that were embedded inside the oscillator in order to perform non-intrusive measurements. In addition, air is used as a working fluid and is fed at high pressures so that the flow is choked at the inlet. The pulsation of the oscillators can reach frequencies of up to 9kHz and it was possible to measure the resulting fluctuations at different points inside the micro-channels. The sensors were able to detect harmonics at up to 50kHz. With this spatial and temporal information, it finally becomes possible to probe the inner dynamics of the micro-meter scale oscillator and to better understand phenomena such as high-frequency microjet switching under highly compressible flow conditions.

Keywords: polysilicon, fluidic-oscillator, temperature-sensor, micro-fabrication

1. Introduction

Although fluidic devices such as the Tesla valve or the turbulence amplifier had already been developed in the 1920's, the field of fluidics truly took off in the late 1950's at the Harry Diamond Laboratory. According to Fabisch [1], the field of fluidics was born in 1957 when physicist Billy Mitchusson Horton realized that a jet of fluid can be controlled by another jet having a significantly smaller momentum. This realization led to the development of the fluidic amplifier. It is the central component in a number of devices such as the fluidic oscillator. Fluidic oscillators are bi-stable devices capable of producing a pulsed flow. They can be used as actuators as well as sensors since their frequency is a function, for instance, of temperature and chemical composition of the working fluid (the report by [2], just to cite one, offers an expansive view of the breadth of applications where oscillators could be found).

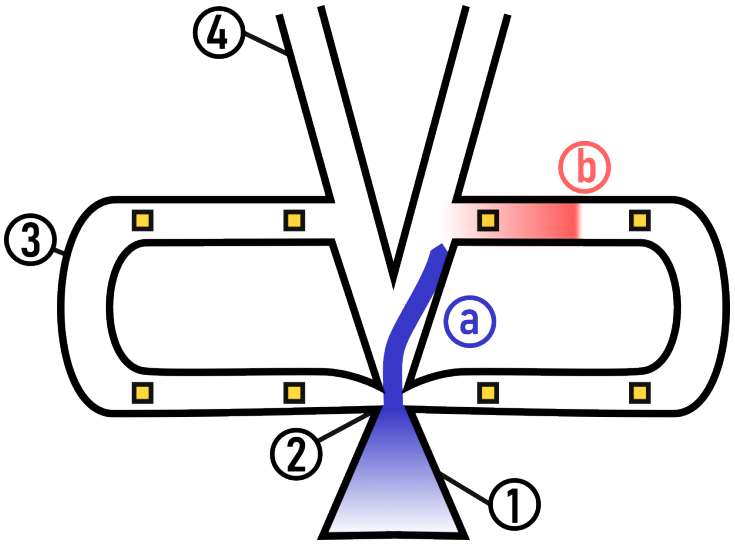

Figure 1: Diagram of the fluidic oscillator/electronic sensors system. Nomenclature: (1) plenum, (2) inlet nozzle, (3) feedback loop, (4) exit channel. Main phenomena: (a) main jet switching, (b) pressure wave propagation. The yellow squares represent the locations of the sensors.

Fluidic oscillators have witnessed renewed interest, especially as flow control devices in aeronautical [3, 4] and thermal [5, 6] applications. The device works by supplying it with compressed air (plenum (1) in Figure 1). A jet issues from the inlet nozzle (2) and is bent towards one side of the device as a

consequence of the Coandă effect on the inclined side wall. The sudden flow on that side produces a pressure wave (b) that propagates in the feedback loop. Once it has crossed the entire length of the feedback loop, it interacts with the main jet and makes it switch to the other side where the same chain of events then take place. In some studies, such as [7], the pressure wave is reflected back through the loop and it is this returning wave that induces switching. Either way, the yellow squares in Figure 1 are signposts for these events and by placing sensors at these locations one could determine what phenomena occur and when.

The same design considered here was previously studied at a sub-millimeter scale [8]. However, little attention has been given to fluidic oscillators at true microscale. Simões et al. [9] used hot-wire anemometers to characterize microfluidic oscillators with air as the working fluid. In order to be able to measure the outlet velocity, they used a design whose outlet channels expand to millimetric dimensions. Yang et al. [10] used fluorescence methods to observed the flow of the liquid inside the oscillator. The inlet was 16 µm wide and 263 µm deep.

Since the flow inside the oscillator is compressible, velocity and pressure fluctuations are accompanied by temperature fluctuations that can be measured in different ways. A number of thermal measurement methods exist such as resistance thermometers or optical thermal imaging. Resistance thermometers such as PT100 or polysilicon-based resistors (e.g., Chang et al. [11]) are prone to self-heating and even though the measurements can be corrected, the dissipated heat can have an effect on the flow. Thermal imaging is also used for liquid flows in microchannels [12] but is not adapted for gas flows. The polysilicon Zener diode sensors presented next, based on the work of [13], are more suited to the present application since they have a high thermal resistivity, low self-heating for a specific range of currents and they are non-intrusive. The idea of using Zener diodes as both thermal sensors and actuators was also recently studied by McAfee et al. [14].

The development of complex microfluidic devices was first made possible by the use of polydimethylsiloxane (PDMS) soft-lithography [15], which is a relatively simple tool for rapid prototyping. A master mold is made using photolithography into which the PDMS is poured and polymerized. The resulting PDMS chips are then bonded over the substrate. In the present application, this technique is not appropriate for a number of reasons. First, PDMS is porous to gases. Second, obtaining aspect ratios of 1:5 or more is challenging [16]. Larger aspect ratios are desirable because jet switching

occurs more readily when the flow is two-dimensional. This observation was made early on during the Fluidics era in the 1960's (e.g. Muller [17]). A different approach altogether consists in using a permanent epoxy dry film that is laminated onto the substrate, instead of the spin-coated liquid resin. For example, Stöhr et al. [18] used TMMF S2000 dry film to produce 2D microchannels which showed a good adhesion between the layers of TMMF and between the dry film and the silicon or glass substrate. In the present work, DF-1000 series dry-film is used and is around ten times less expensive than both SU-8 and TMMF S2000 for the same layer thickness, and three times faster to process than SU-8. Courson et al. [19] showed that using DF-1000 can accurately produce the desired patterns, with residual stresses and optical properties comparable to those of SU-8 photoresist.

The present work aims to present a proof of concept of a microfluidic oscillator, also known as a pulsed jet actuator (PJA), with sensitive, rapid and non-intrusive embedded sensors. Owing to the size of the microchannels and the weak temperature fluctuations, highly sensitive temperature sensors are required to extract useful data about the internal flow. It is also important to have measured currents strong enough ($I \approx 1\,\mu\text{A}$) to be easily picked up and processed. These constraints have guided the design and optimization of the thermal sensors. The size of the sensors and the length of the $pn-$junctions were also determining factors in this regard. What makes the current iteration of these sensors stand out from its predecessor is the partial suspension of the sensing area. The was necessary to reduce thermal inertia and accommodate the high-frequency fluctuations achieved by the device. A large portion of the work presented here is concerned with the manufacturing and testing of the fluidic/electronic chip with some preliminary results on the functioning of the oscillator. The characteristic dimension of a fluidic oscillator is the width of its inlet section. In the present work, all of the designs have an inlet width of 20 µm with an aspect ratio going from 1:1.25 to 1:5. For comparison, in Yang et al. [10], the inlet's width and depth were 16 µm and 263 µm, respectively, and about 280 µm and 100 µm in Simões et al. [9] (outlet diameter of the supply nozzle). Finally, these devices could also prove useful in cooling applications. For instance, Huang et al. [20] simulated pulsed microjets that impinge on a heat sink in order to cool it down. The study was numerical and the pulsations were produced using a time-dependent inlet boundary condition. Microfluidic oscillators could be a suitable candidate to produce the pulsed flow in actual experiments.

2. Materials and Methods

2.1. Microfluidic layer

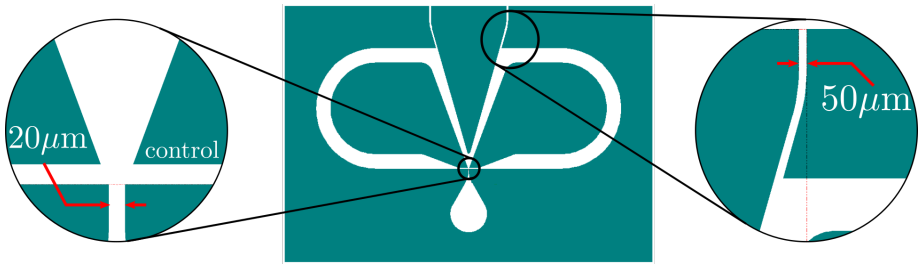

(a) (B1): $L_f = 11\,000\,\mu\text{m}$

(b) (B2): $L_f = 45\,000\,\mu\text{m}$

Figure 2: Different oscillator designs used for producing pulsed microjets. The total length of the feedback loops (both sides) is included for each design.

Two designs were implemented (mask drawings of the channel patterns are shown in Figure 2), to assess the effect of feedback loop length on the frequency response. The first design, dubbed 'B1' (Figure 2a) has the shortest feedback loops of the two designs, and, based on dimensional arguments, should have a frequency roughly ten times that of its large-scale counterpart, i.e., around 10 kHz (refer to [8] for a study on millimeter-scale oscillators with the same design). This assumes that both the pressure wave propagation time and the switching time are proportional to the dimensions of the device (see Figure 1 and accompanying text). For the pressure wave propagation time this should be the case if the speed of sound remains relatively unchanged. For the switching time, this has not yet been proven. Seeing as the effects of scale reduction on the switching mechanism are currently unknown, this value merely serves as a rough estimate. Experimental and numerical studies on switching time in sub-millimeter scale devices can be found in [8] and [21], respectively. To our knowledge, there are no studies reported in the literature on the characteristics of a truly microfluidic oscillator with air as working fluid and a choked flow at the inlet. The second design, 'B2' (Figure 2b), was

identical to the first except for its longer feedback loops that should bring the frequency down to around 2.5 kHz.

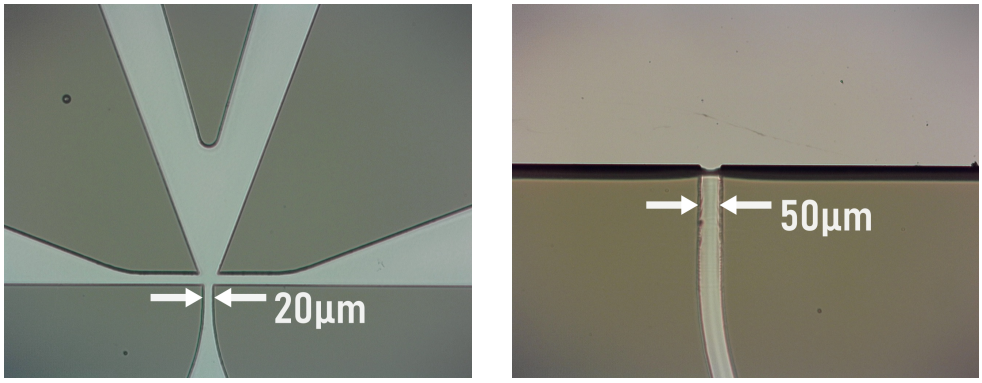

(a) (b)

Figure 3: Microscope images of (a) the narrowest channel of the oscillator (throat width = 20 µm), and (b) an exit channel, which correspond to the inset detailed views in Figure 2a

The microfluidic oscillators were made by stacking several layers of epoxy dry-film onto 4" silicon wafers (SiP 1701). For the prototypes having a channel depth of 50 µm, a layer of DF1050 (50 µm) is laminated onto the substrate. The desired pattern is transferred from the mask to the dry film layer by exposing it to UV radiation. A good resolution was obtained for the narrowest channel in the oscillator at the inlet (Figure 3a). Similarly, the 50 µm-wide exits were well-rendered (Figure 3b).

2.2. Sensing layer

An array of temperature sensors is implanted on an insulating silicon substrate before setting the microfluidic channels. These sensors are intended to pick up on weak temperature fluctuations resulting from pressure waves propagating through the oscillator. Other types of micro-sensors, such as pressure sensors, are more prone to damage and have significantly longer response times. The temperature sensors adapted for this study were developed at the Laboratory for Analysis and Architecture of Systems (LAAS, Toulouse, France) [13] and have a high thermal sensitivity and small response times. In the current iteration, the sensing elements were partially suspended over the substrate to minimize thermal inertia. The sensors were placed at

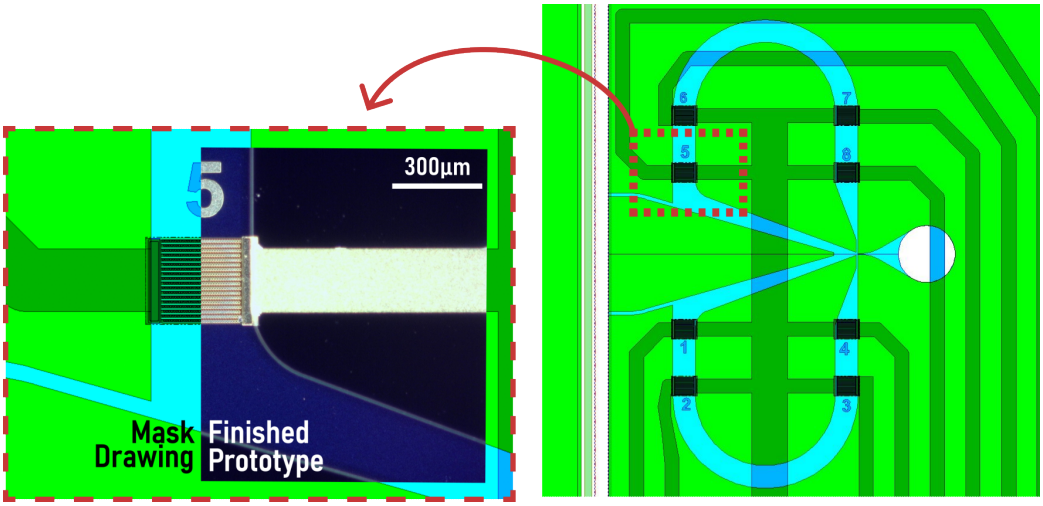

Figure 4: Overlaid mask drawings of the different layers that make up the microfluidic/electronic chip showing the layout of the sensors in a B1 design with a detailed view of one of the sensors. A microscope image of the actual sensor that was produced is overlaid.

the inlet and outlet of each feedback loop and along its length according to the layout in Figure 4 for B1. A similar layout was used for B2.

The process described in this section resulted in $300\,\mu\text{m} \times 300\,\mu\text{m}$ thermal sensors placed inside the microchannels with high accuracy ($\approx 1\,\mu\text{m}$) as attested by the detailed view in Figure 4 which compares part of a drawing of the microfluidic/electronic chip with a dark field image of the actual device that was made. The excellent alignment is guaranteed by the photolithography step, which would not be possible with processes involving PDMS.

The sensors were Zener junctions (P^+N^{++}) in a polycrystalline silicon film deposited on a passivated silicon wafer. In brief, the process starts with a Boron implantation ($p-$type) into the entire polysilicon film. The $n-$type regions were then patterned onto a photoresist layer by photolithography followed by ion implantation of Phosphorus into the $p-$type region. The donor concentration N_D was significantly higher than the acceptor concentration N_A. With this condition ($N_D \gg N_A$) in mind, the following approximation of the width W_T of the depletion region could be made:

$$W_T = \sqrt{\frac{2\varepsilon V_{bi}}{q}\left(\frac{N_A + N_D}{N_A N_D}\right)} \approx \sqrt{\frac{2\epsilon V_{bi}}{qN_A}} = w_T \tag{1}$$

where ε is the permittivity of the polysilicon film, V_{bi} the potential barrier of the junction, q the elementary charge and w_T the width of the depletion region on the $p-$type side. As a result, the depletion region extends almost entirely into the $p-$region and the properties of the $P^+N^{++}-$junction, which acts as a Zener diode, were only determined by the concentration N_A of the $p-$type dopant, which is tightly controlled by the Boron implantation dose.

Depending on the applied current, this Zener diode, in reverse bias, can function as either a thermal actuator or sensor. The semi-logarithmic plot of a typical characteristic curve for this sensor is shown in Figure 5, and is used to illustrate the following operating modes:

1. **Low current:** below a current of around 10 nA, the electrons cannot overcome the barrier potential of the $P^+N^{++}-$junction. As a consequence, a very weak current goes through the layers surrounding the polysilicon (e.g., the substrate beneath the polysilicon film).
2. **Thermal sensor:** for intermediate values of the current ($10\,\text{nA} < I < 10\,\mu\text{A}$), the depletion region has a thickness of a few nanometers through which tunneling conduction can occur. The characteristic curve is sensitive to temperature variations in this mode and reaches a peak sensitivity $S_V \approx -75\,\text{mV}\,^\circ\text{C}^{-1}$ (Figure 5, blue curve). To put this value into perspective, K-type thermocouples can only reach a sensitivity of about $40\,\mu\text{V}\,^\circ\text{C}^{-1}$.
3. **Thermal actuator:** Above a current of around 20 µA, the electric field is enough for electron conduction through the barrier. The electrons flow through the entire volume of the polysilicon film. This conduction mode is dubbed the "volume conduction mode". The element dissipates heat with a resistance R_S. Surface and stray conduction still occur, but are negligible compared to volume conduction. Although the voltage remains sensitive to temperature changes, the dissipation of heat would hinder temperature measurements and so the element cannot be used as a sensor in this mode.

The sensor can be operated in either constant current or constant voltage mode. In constant current mode, for $I = 1\,\mu\text{A}$, there is a voltage decrease

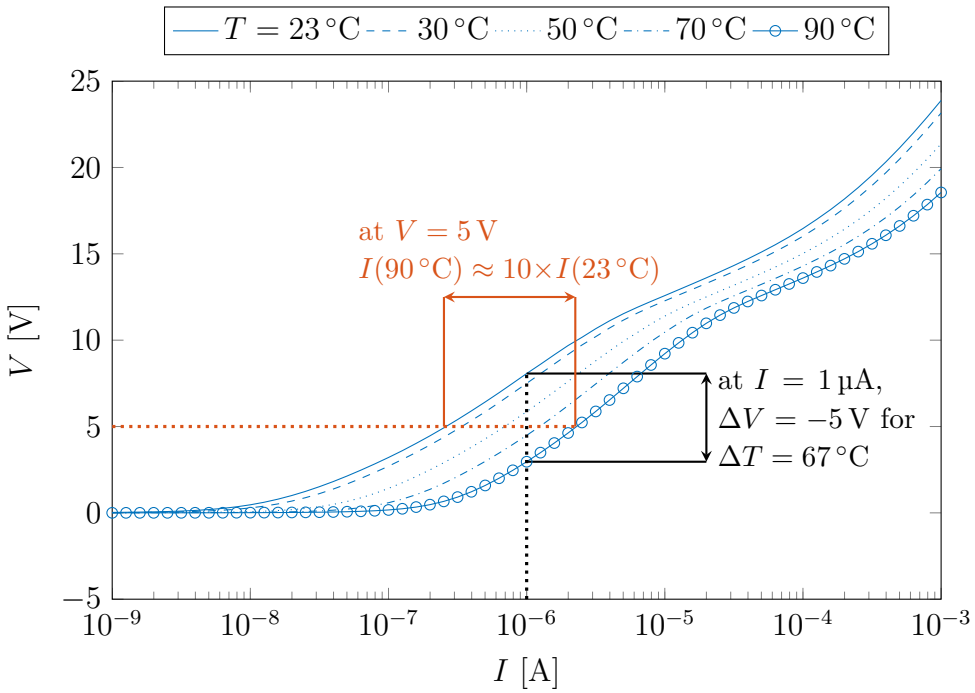

Figure 5: Example of a characteristic curve for the sensor.

of 5 V when the temperature is increased from 23 to 90 °C which implies a sensitivity of more than 70 mV °C^{-1}. In comparison, K-type thermocouples have a typical sensitivity of around 50 µV °C^{-1}, in other terms, three orders of magnitude lower than the sensors used here. As will become apparent in Section 3 and in Appendix B, the sensor voltage response to temperature is nearly linear in the detection zone. On the other hand, in constant voltage mode, for $V = 5\,\mathrm{V}$, the current increases tenfold for the same range of temperatures. The exponential behavior of the current sensitivity is comparable to that of Compensated Thermal Neutron (CTN) sensors. This high sensitivity will be leveraged in order to detect the weak temperature fluctuations in the channels and it explains why a transimpedance amplifier was used in the amplification circuit in Appendix A.

Since high sensitivity is guaranteed for these Zener sensors, additional technological development is still needed to significantly reduce their response time. If the sensor is made directly on a silicon wafer, the thermal inertia of silicon prevents it from reaching response times of less than a millisecond and so, they would not be able to pick up kilohertz fluctuations. For this

reason, the polysilicon layer was locally suspended by doing a selective aqueous attack (Buffer HF) of an underlying sacrificial SiO_2 layer. The duration of the etching was a crucial factor. Long etching times result in silicon oxide pillars so thin that they could not support the overhanging polysilicon film. On the other hand, if the oxide layer is not etched long enough, the thermal inertia remains significant, thus limiting the response time to a few milliseconds, incompatible with our fast-thermal instrumentation needs ($< 10\,\mu s$). A trade-off between mechanical strength and low thermal inertia must be found. In the following, the description of the process is broken down into three parts, namely, substrate preparation, implementation of the sensor and finally wet etching.

Preparing the substrate

The process is done on a 4" diameter, 400 µm Silicon (Si) wafer that is 400 µm thick and has a high resistivity (HR) of $\rho \approx 4000\,\Omega\,cm$. High resistivity wafers were chosen to limit parasitic currents (resistive and capacitive conduction) between the sensor and its long interconnections on the one hand, and the substrate on the other. The preliminary steps are as follows:

1. Deposition of a 2 µm-thick layer of silicon oxide SiO_2 by Plasma-enhanced chemical vapor deposition (PECVD) at 300 °C. This layer will be etched at the very end of the entire process in order to suspend the junctions.
2. Low pressure chemical vapor deposition (LPCVD) of 100 nm of Si_3N_4 which will serve as a protective layer during HF etching at the end.
3. LPCVD of 300 nm of polysilicon at 605 °C.
4. Ion implantation of Boron (P doping) with an ion acceleration energy of $E_B = 30\,keV$ over all the wafer surface. The dopant concentration was adjusted to optimize the sensibility at a current polarization of about 1 µA (to lower power consumption and prevent self-heating). The acceptor concentration is $N_A \approx 2 \times 10^{18}\,cm^{-3}$. Further details on how the concentration was determined can be found in Appendix B.
5. Finally, a silicon dioxide mask for high temperature diffusion (at about 1000 °C is deposited by PECVD at 300 °C (250 nm).

An illustration of the prepared wafers is shown in Figure 6a. Steps 1-4 are done on both sides of the wafer in order to balance out the thermo-mechanical stresses inside the layers and reduce wafer deformation.

Producing the thermal sensor

The next part of the process is comprised of 5 photolithography steps, the first four to pattern the P^+, N^{++}, polysilicon and metal layers. The fifth photolithography step is followed by the selective aqueous attack.

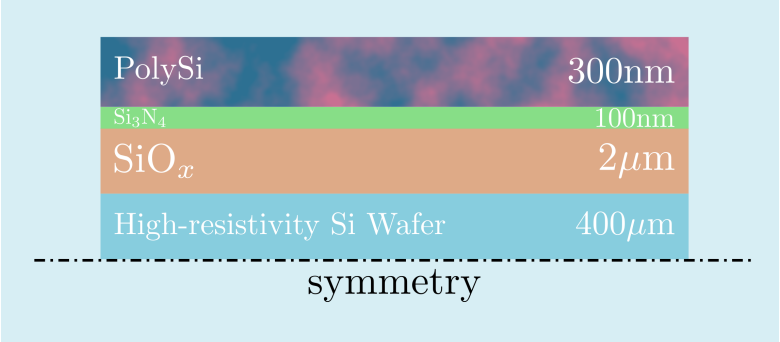

(a) Preparation

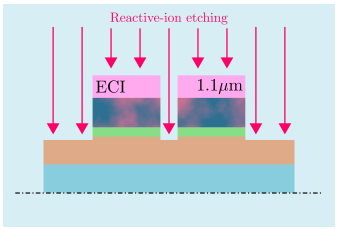

(b) Step 6

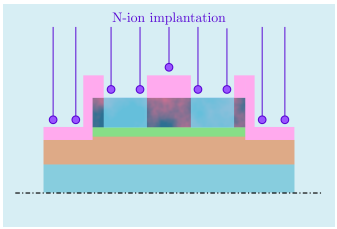

(c) Step 7

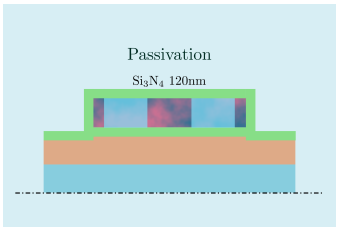

(d) Step 8

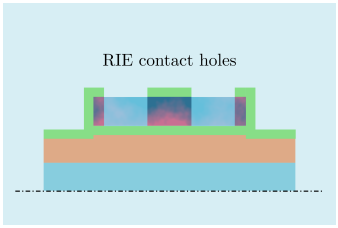

(e) Step 10

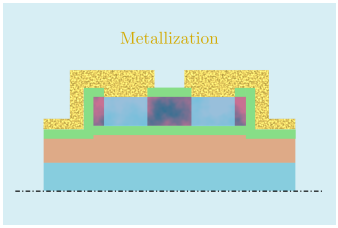

(f) Step 11

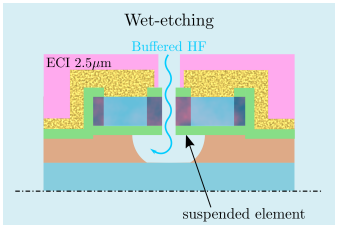

(g) Step 13

Figure 6: Microstructuring process of the temperature sensors that will be embedded in the microfluidic oscillator.

The remaining steps of the process, illustrated in Figures 6b to 6g, are as follows:

6. **Photolithography 1, etching out the sensors**: Patterning of the polysilicon and silicon nitride layers by photolithography of a 1.1 µm

ECI photoresist, followed by reactive ion etching (RIE). The resin is then removed (acetone and plasma O_2).

7. **Photolithography 2, N^{++} zones by ion implantation of phosphorus**: the N^{++} zones are patterned into a 2.5 µm ECI layer followed by an ion implantation of phosphorus with an ion acceleration energy $E_{ph} = 30\,\text{keV}$ and a dose of $6 \times 10^{16}\,\text{cm}^{-2}$ to obtain a donor concentration $N_D \approx 2 \times 10^{21}\,\text{cm}^{-3}$.
8. **Passivation layer**: LPCVD of an 80 nm silicon nitride (Si_3N_4) passivation layer at 700 °C.
9. **Annealing and dopant activation:** Baking at 1000 °C for 30 minutes with N_2 is required for both activated Boron and Phosphorus implanted ions.
10. **Photolithography 3, opening of contact aperture**: Deposition of a 1.1 µm ECI photoresist, patterning of the contact apertures areas by photolithograpy followed by reactive ion etching of the silicon nitride layer and partly into the polysilicon layer to ensure electrical contact in the next step.
11. **Photolithography 4, metallization patterns**: Chromium/Gold (Cr 50 nm, Au 300 nm) metallization patterned by lift-off to create interconnections capable of resisting the HF buffer.
12. **Alloying:** Baking at 250 °C for 1 hour with N_2H_2 to enhance the adherence of the metallic layer.
13. **Photolithography 5, wet etch**: A 2.5 µm layer of ECI is deposited to protect the sensors from the final etch using a buffered etchant in an ultrasonic vessel. The etching time determines the size of the cavities in the sacrificial SiO_2 layer.

The final, and arguably most crucial step of the microstructuring process is the wet-etching. After several tests, it was determined that an etching time of 40 min at around 27 °C was needed to remove all but 2 µm wide strips of the SiO_2 layer. These strips, or anchors, support the polysilicon layer. Images of the 300 µm × 300 µm sensor with openings for the final Buffered Oxide Etch (BOE) step are presented in Figure 7. The green area is the polysilicon layer and the lighter color is where the sacrificial silicon oxide layer underneath it was etched. The dark circles inside the light areas are the holes through which the BOE reaches the sacrificial oxide layer. Some defects in the passivation layer can be seen in Figure 7a, however this layer plays no role in temperature detection, it only serves to encase the sensor. If the

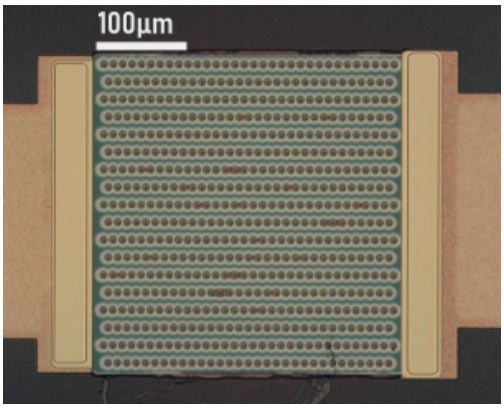

(a) Opening holes for contact and final wet-etching (step 13)

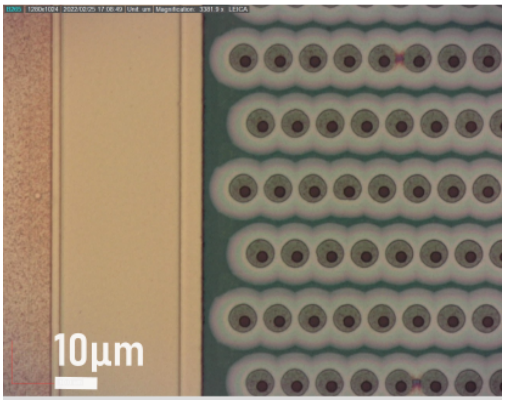

(b) Detailed view of the suspensed zone (lighter regions)

Figure 7: Microscope images of the suspended sensors. This version of the sensor has holes in the polysilicon to enable partial removal of the SiO_x layer.

wet-etching time is prolonged, this phenomenon becomes more pronounced and the passivation layer even starts to scale off. Upon closer inspection of Figure 7b, this slight defect can be seen between the third and fourth holes from the right in the top row and the fifth and sixth holes from the left of the bottom row. It can easily be ascertained that the defects are superficial. It is also worth noting here that Figure 7a puts into perspective the size of the apertures. The channels are 300 µm wide and the air flows, with a Reynolds number of the order of 100, in a direction parallel to the apertures, each of which has a diameter of only 3 µm. What's more, the depth of the cavities is only 2 µm. All of this to say that the sensors do not constitute in any way an obstacle to the flow and as such the measurement are non-intrusive.

PN−junction suspension via wet-etching

The wafers were etched for 40 min so that the $pn-$junction is completely suspended. The reader is referred to Appendix C for more details on how the etching time was determined and what factors were involved. Using a focused ion beam (FIB) parts of the circuit were gradually removed to reveal the stacked layers and assess the final wet etch. As can be seen in Figure 8a, the remaining pillars of the oxide layer are sufficiently wide to ensure stable support. A closer view of one of the openings is presented in Figure 8b. The image was colorized to indicate the $p-$ (blue) and $n-$regions (red). The

junctions are clearly detached from the substrate. The total width of the emptied region at the cross section shown in these figures is roughly 9.50 µm

2.3. Chip assembly

The silicon wafer, on which the sensors and microfluidic channels were made, is diced with a diamond saw and the parts were glued onto dedicated PCBs. To avoid damaging the dry film layers, a space must be left between the sawed edge of the silicon substrate and the edge of the dry film. At the same time, the wafer needed to be cut as close as possible to the outlet of the oscillator to reduce the interaction between the microjets exiting the channels and the wafer. A margin of less than 50 µm was chosen as a reasonable compromise (Figure 9, blue). The chip was then connected to the PCB via wire bonding (Figure 9, red). Finally, the wires were protected with conformal coating which was cured by UV light. A rubber O-ring ensured a leak-free connection between the oscillator inlet and the casing. A push-in pneumatic fitting connected the device to the service air.

3. Sensor electrical tests and experimental results

3.1. Before Buffered Oxide Etching (BOE)

Before partially etching the sacrificial layer beneath the junctions, the current-voltage characteristics of the different sensors were first measured and plotted. In addition to the width of the junction and the concentration

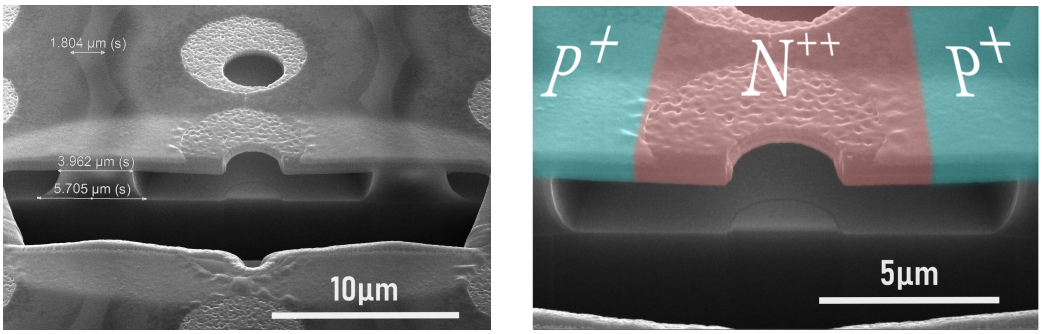

(a) (b)

Figure 8: (a) SEM of the suspended regions after removal of parts of the sensor using a focused ion beam (FIB). (b) A close-up of the sensor which was colorized to show the position of the $pn-$junction

of N_A acceptor atoms, the sensitivity to light and the presence of holes in the polysilicon layer can affect the characteristics of the sensors. The first electrical tests consisted in measuring the current-voltage characteristic of a number of identical $300 \times 300\,\mu m^2$ sensors with a p doping level of $N_A \approx 2 \times 10^{18}\,cm^{-3}$. These tests were performed on the same wafer and under the same operating conditions (room temperature, absence of light, etc.). The dispersion of the data around the mean curve does not exceed 1.5% in the detection ($I = 0.1$ to $10\,\mu A$, Figure 10a) and actuation ($I \geq 10\,\mu A$) ranges. The dispersion reaches 12% or more for current less than 10 nA.

The depletion region extends almost entirely into the $p-$region because of the high levels of acceptor concentration. The holes in the polysilicon layer, whose purpose is to provide a path for the final wet-etching step, were intentionally placed in the $n-$region to avoid interference with the depletion

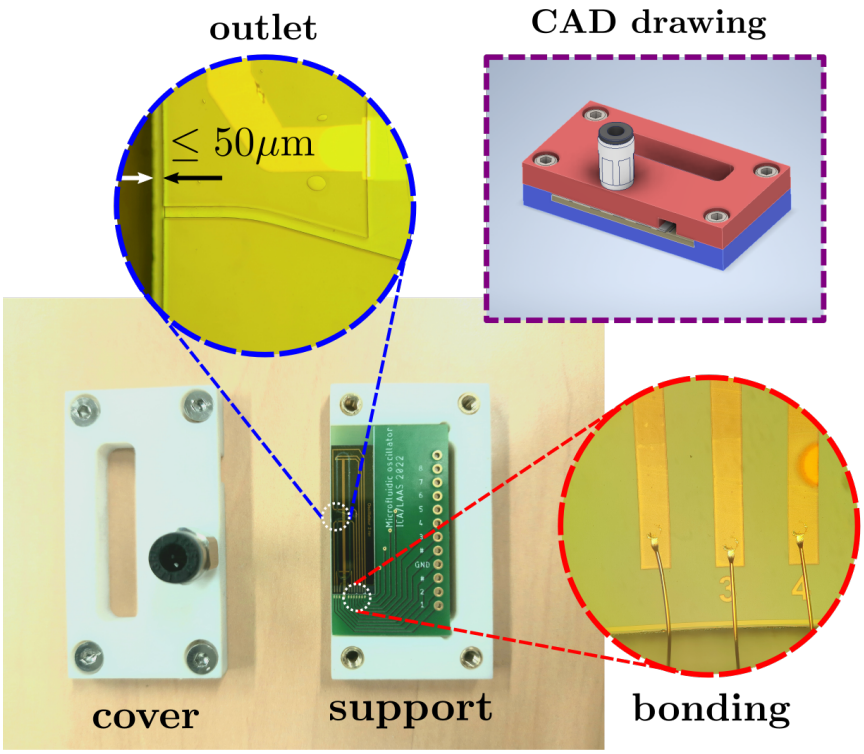

Figure 9: Chip/PCB/casing assembly with detailed views of the chip-to-PCB bonding wires (red) and of the diced edge of the wafer in front of the micro-oscillator's exit (blue) and the CAD drawing of the assembly (purple).

layer. In addition, these holes do not alter the charge density, the cross section or the length of the $pn-$junction. So in principle, placing the openings in the $n-$region should not have an effect on the current-voltage characteristic in the detection region. This is not necessarily the case for the volume conduction region, since the holes alter the resistance of the $n-$region. This was verified for a number of sensor-pairs and an example is shown in Figure 10b.

To sum up, these diodes can be produced consistently and are not affected in any significant way by either light or openings in the $n-$doped regions. However, they are highly sensitive to temperature variations. For a given voltage level, the current increases with temperature, leading to a noticeable change in the current-voltage characteristic, especially in the detection range (Figure 11). In the volume conduction range, the junction switches to a thermal actuation mode whereby it produces enough heat to alter its own temperature, making it unsuitable as a sensing element. The transition between the surface and volume conduction modes occurs when the slopes of the V/I characteristic change. The highest current level at which the tran-

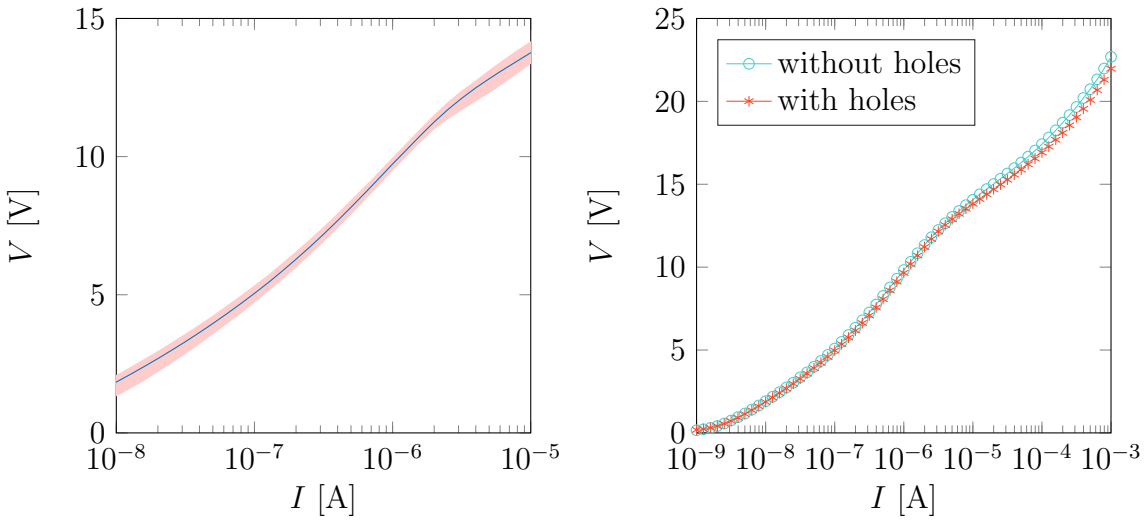

Figure 10: Plots showing (a) the mean characteristic curve with dispersion bands (red) from 14 300 µm × 300 µm- sensors from the same wafer ($D \approx 7 \times 10^{13}\,\mathrm{cm}^{-2}$) with BOE openings and (b) current-voltage characteristics of two sensors with and without openings for the final wet-etching step.

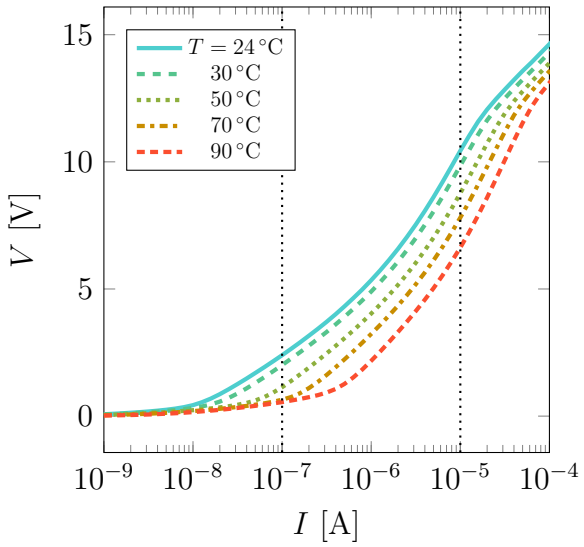

Figure 11: Plot of the V/I characteristic curves for the 300µm × 300µm sensor at different temperatures.

sition happens was obtained for $D \approx 7 \times 10^{13}\,\mathrm{cm}^{-2}$ (compare Figure 11 to Figure B.18) and is equal to approximately $I = 10\,\mu\mathrm{A}$. In the remaining cases (Appendix B), the detection range extends to around $I = 2\,\mu\mathrm{A}$.

Using these V/I characteristics, the sensors' thermal sensitivity can be estimated for each temperature range (Figure B.19c). The sensitivity curves for the different doping levels all exhibit the same behavior. For low currents, the sensitivity is nearly zero but begins to rapidly rise as surface conduction starts to take over. In the detection zone, where the leakage current becomes relatively negligible but volume conduction is not yet predominant, the increase in sensitivity slows down, sometimes reaching a plateau (e.g., Figure B.19a). The peak sensitivity is achieved in this range and has a typical value of -60 to $-80\,\mathrm{mV\,°C^{-1}}$. To put these values into perspective, type K thermocouples (Chromel/Alumel) usually have a thermal sensitivity of only $40\,\mu\mathrm{V\,°C^{-1}}$ which is three orders of magnitude lower than for the sensors produced here.

3.2. Post-BOE

The characteristics were again measured at different temperatures in order to assess the thermal sensitivity of the post-BOE sensors (Figure 12). A clear shift in the curve can be noticed as the temperature is increased. The

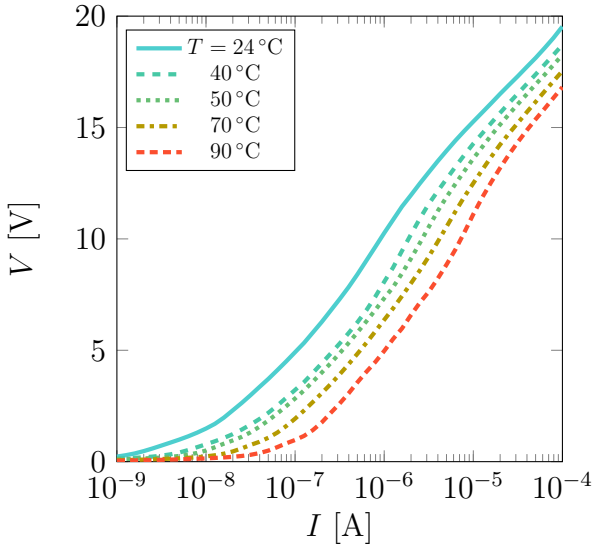

Figure 12: Voltage/current characteristic of the sensors after the wet etch for different temperatures.

results show that the peak sensitivity is nearly the same as it was prior to the etch. In the low temperature range, the sensitivity remains close to its value before the BOE for $I \approx 1\,\mu\mathrm{A}$ (the sensitivity curves are not shown here for brevity's sake).

3.3. Preliminary Acoustic Measurements

The acoustic waves exiting the microfluidic oscillators are strong enough and their tones distinct enough to be picked up by any microphone and the data analyzed to estimate the frequency. A series of prototypes were first produced without the thermal instrumentation. The acoustic measurements can then be used as a simple diagnostic method to check if the oscillators work at this scale, before performing the entire sensor fabrication process detailed in Section 2.2. Prototypes having constant depths of 25 and 50 µm were produced and their frequency was estimated as that of the audible tones they emit. The 25-micron-deep designs did not seem to function at all. This is unsurprising seeing as the aspect ratio of the inlet section is less than 2. On the other hand, oscillators B1 (having the shortest feedback loops) and B2 (with a similar feedback loop design as B1, but longer) with a depth of 50 microns emit a clear sound that can easily be picked up by a microphone (Figure 13).

Their frequencies are, roughly speaking, ten times higher than those of their larger scale equivalents ([8]). Seeing as the deeper channels showed more promise, and after the sensor arrays were produced, an additional series of oscillators was made with a depth of 100 microns. In this case, both designs produced clear, measurable tones.

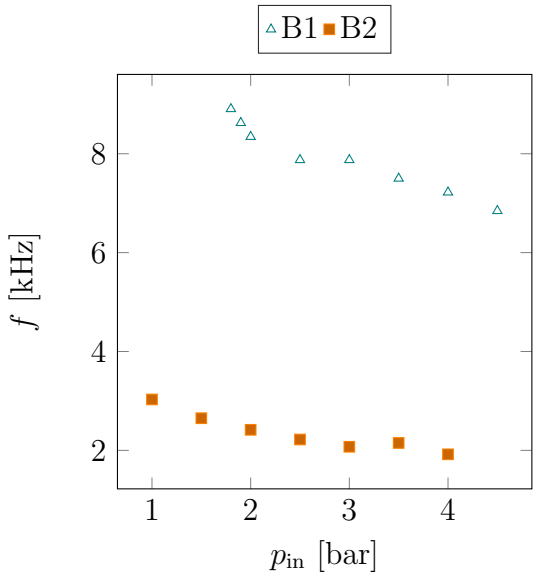

Figure 13: Frequency detected using a microphone versus inlet pressure for the oscillators with a depth of 100 µm.

Comparing the frequency curves for B1 with a depth of 50 µm (Figure 14) and 100 µm (Figure 13), a striking difference between the shape of the curves and the values of the frequency can be observed. Whereas the frequency of the 50 µm-deep version peaks at around $p_{\text{in}} = 2.3$ bar before reaching a nearly constant value for higher pressures, the frequency for 100 µm decreases monotonically across the entire range of pressures. Similarly, the frequency of B2 when its depth is 100 µm is lower than had been noted for the shallower oscillator. For oscillator B1, the shape of the frequency curve could be explained by a change in jet switching time in response to different inlet pressures. A somewhat similar behavior was also observed, albeit in a different pressure range, for the large-scale prototypes in previous studies [8].

For Oscillator B2 (Figure 14), the tone becomes distinct at $p_{\text{in}} \geq 3.3$ bar, and its frequency decreases slightly in the range of pressures considered, but remains close to 4300 Hz. Here again, above a certain pressure, the tone

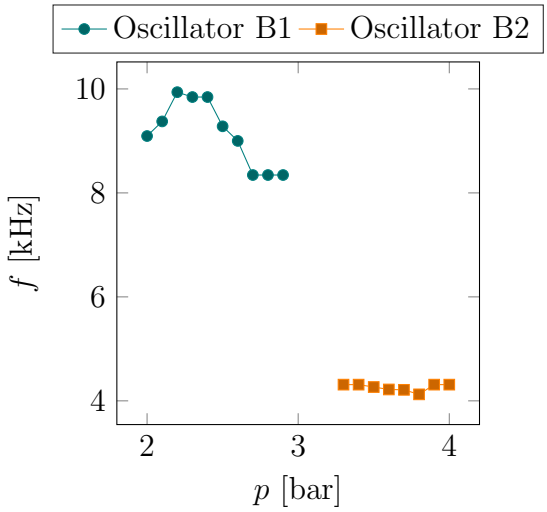

Figure 14: Detected frequency of Oscillators B1 and B2 with a depth of 50 µm for different inlet pressures.

becomes difficult to distinguish from the noise.

The following table summarizes the frequency measurements:

Table 1: Frequency ranges detected using a microphone for different oscillator designs and channel depths.

		Channel depth		
Prototype	L_f	25 µm	50 µm	100 µm
B1	11 mm	–	8.41 – 9.92 kHz	6.85 – 8.9 kHz
B2	45 mm	–	4.12 – 4.31 kHz	1.93 – 3.03 kHz

3.4. Measurements using the thermal sensors

Having proven the mechanical strength of the sensors as well as the repeatability of their fabrication process by performing extensive electrical tests, it was time to use them to measure fluctuations inside an oscillator. Figure 15 shows an example of a temporal signal measured at the inlet of the left feedback loop of 'B1' oscillator, for $p_{\text{in}} = 2.5$ bar. The sensors were operated at constant voltage to obtain the highest possible sensitivity, and the current was amplified using the circuit shown in Appendix A.

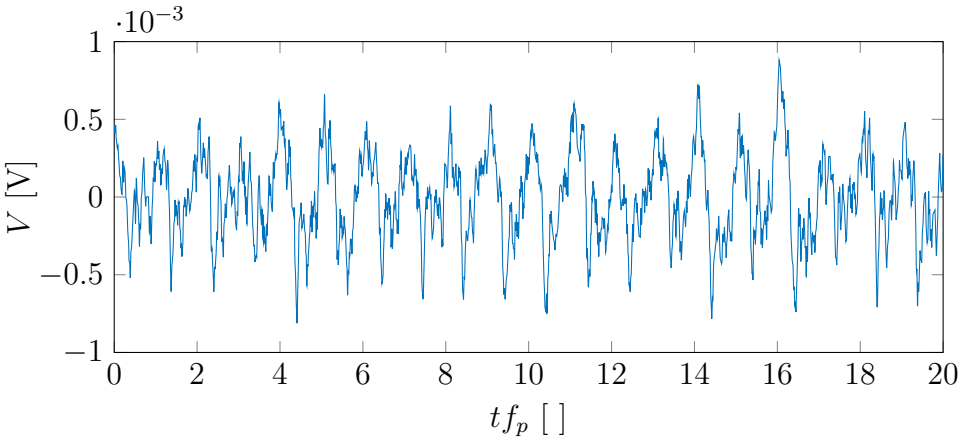

Figure 15: Measured voltage signal as a function of dimensionless time tf_p, where f_p is the pulsation frequency.

In Figure 16, the plot of the Fast Fourier Transform (FFT) of the previous signal exhibits seven distinct peaks that stand out from the surrounding noise. The first peak corresponds to the fundamental frequency of the oscillator and is about 25 dB above the surrounding noise.

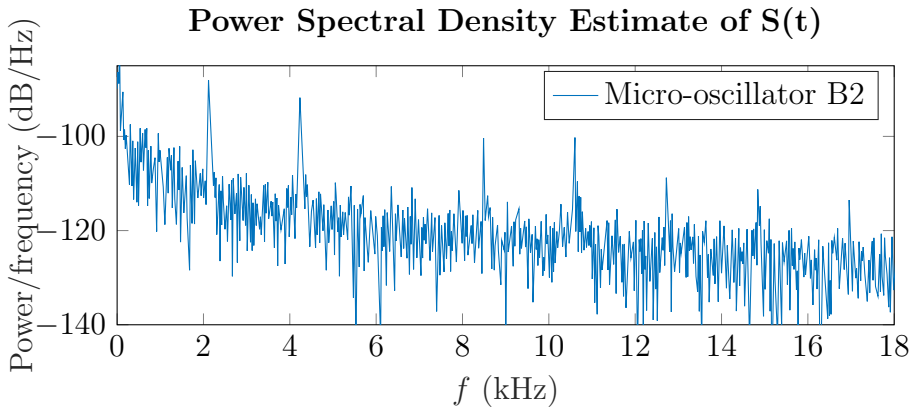

Figure 16: Single-sided FFT of the amplified signal from one microsensor inside of the 100 µm-deep 'B2' oscillator with inlet pressure $p_{\text{in}} = 2.5$ bar (see Table 1).

Similar results within the same range of inlet pressures were also obtained but are not shown here for the sake of brevity. Moreover, for B1, the frequencies deduced from the temperature signals is identical to what was obtained from the audio data to within three significant figures, so the results in Table

1 and Figure 13 remain valid. With the help of an amplification circuit (detailed in the Appendix), the acquired signal clearly stands out from the noise, as attested by the 6 harmonics that can be seen in Figure 16. The work presented here demonstrates that the fluctuations inside the micro-oscillators, which stem from minute and rapid temperature/pressure variations, can be detected using micro-sensors that were produced from scratch.

4. Summary and Conclusion

The entire process of developing, producing and testing microfluidic oscillators with integrated, custom-built, non-intrusive instrumentation was presented. Of particular interest was the attempt to reduce the thermal inertia of a polysilicon based thermal sensor by suspending its temperature-sensitive regions over the substrate via wet-etching. This step is not only feasible and controllable, but the suspended structures are not damaged during the following steps which included applying high pressures and temperatures on the wafer in order to laminate layers of dry-film. A number of oscillators, having different channel depths, were tested. The aspect ratio of the inlet cross section plays a crucial role in determining whether or not the oscillators could function and has an effect on the frequency of pulsation. The final assembly includes the chip with the suspended sensors and microfluidic channels, the casing used to encapsulate the chip and to connect pneumatic fittings for the inlet supply and finally the circuitry used to amplify the signal from the sensors. This highly compact system only requires compressed air and an oscilloscope to run. Preliminary tests have shown that it is possible to detect high-frequency, low amplitude fluctuations using these sensors, thus providing a proof of concept of these instrumented electro-microfluidic chips.

Two points still need to be addressed in the future, the gain from suspending the sensors and the interpretation of the measured signals. Regarding the first point, the signals measured using the suspended and non-suspended sensors need to be compared and the improvement in response time, if any, assessed. On a related note, the pulsed jets produced by the micro-oscillators can be used to cool electronic components in an impinging jet configuration. Therefore, it is also of interest to calibrate these sensors so that they could be used outside the oscillator to quantitatively evaluate cooling performance on a heated impingement surface.

As for the interpretation of the results, CFD simulations of the flow inside the oscillator would help in understanding the phenomena underlying the

features seen in the measured signals. With that correspondence established, the signals can be used to compute such quantities as the rapid switching time of the supersonic micro-jet at the inlet of the oscillator.

5. Acknowledgments

Technological realizations were partly supported by the French RENATECH network

Appendix A. Signal Amplification

Figure A.17 diagrams the amplification circuit which provides an amplified voltage output from a micro-ampere current input going through the micro-sensor (i.e., Figure 12). Amplification occurs in two stages, the first consisting of a transimpedance amplifier (TIA, current to voltage converter) and the second of an operational amplifier. In the interest of clarity, certain parts of the circuit, pertaining to powering the operational amplifiers, were not shown. The response of the sensor is nearly linear in the detection region. Nevertheless, the choice fell on operating the sensor at constant voltage since the current response, although non-linear, is much more sensitive to temperature fluctuations.

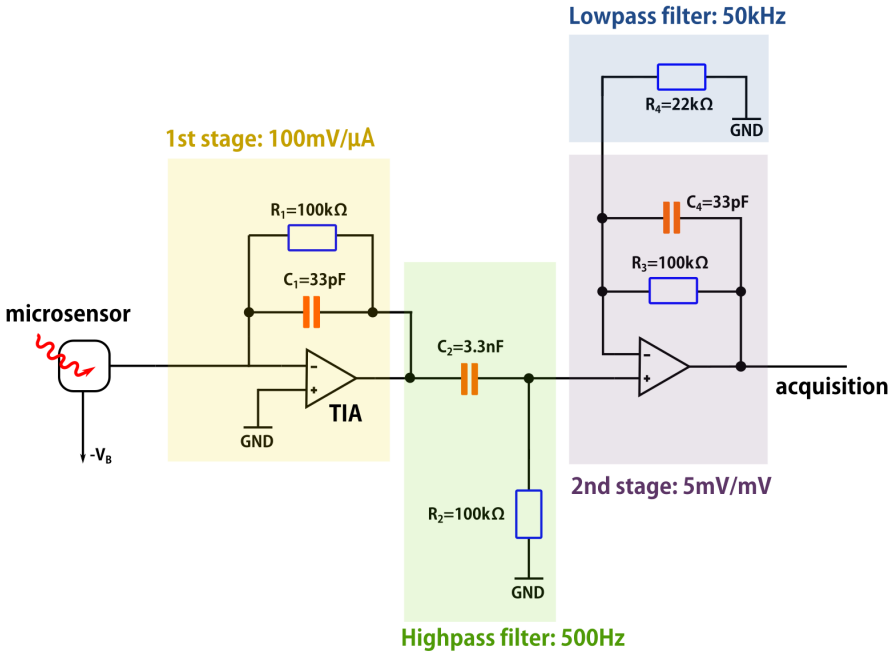

Figure A.17: Amplifier circuit that provides an increased voltage output from a current input from the microsensor.

Appendix B. Choice of dopant concentration

The doping level of the P-regions plays an important role in determining the measurable current passing through the sensors.

Considering different dopant concentrations helped determine which one led to the detection region with the highest current. As can be seen from

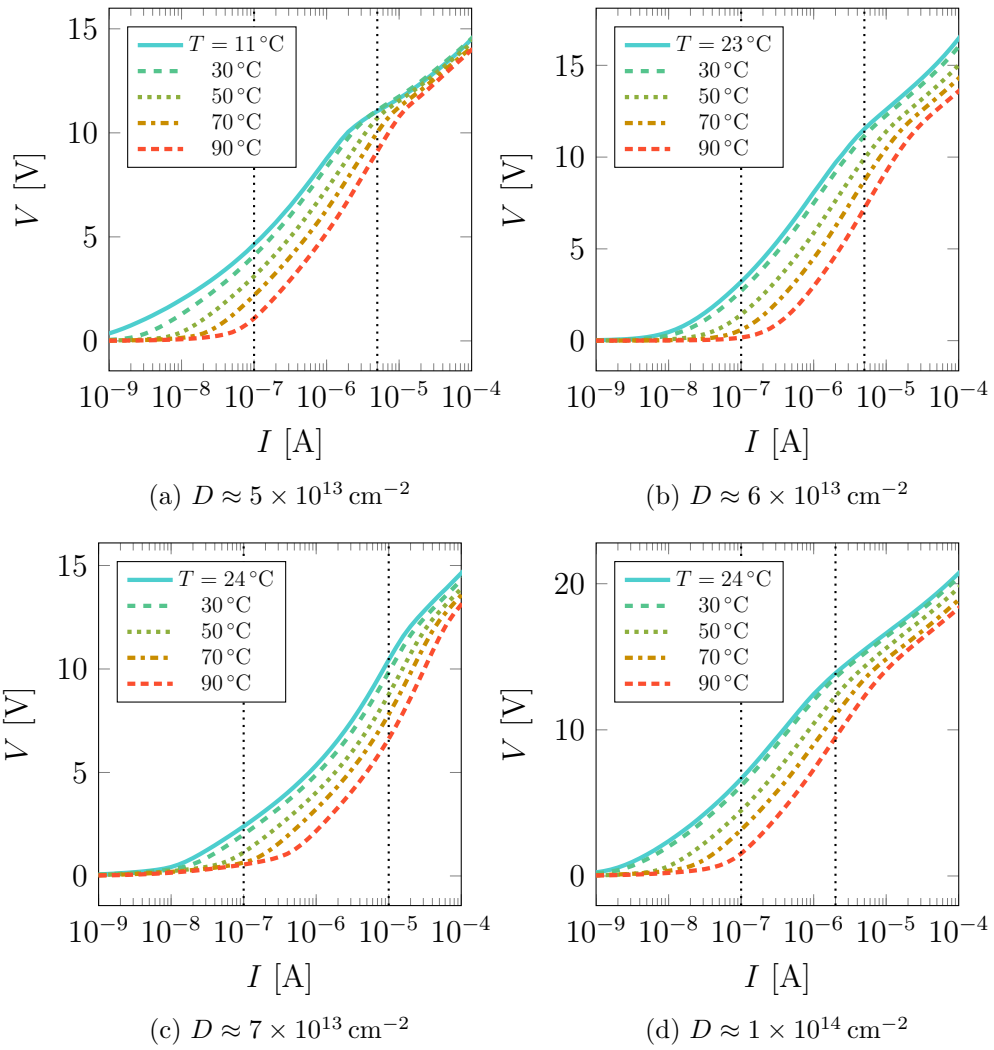

(a) $D \approx 5 \times 10^{13}\,\mathrm{cm}^{-2}$ (b) $D \approx 6 \times 10^{13}\,\mathrm{cm}^{-2}$

(c) $D \approx 7 \times 10^{13}\,\mathrm{cm}^{-2}$ (d) $D \approx 1 \times 10^{14}\,\mathrm{cm}^{-2}$

Figure B.18: V/I characteristic curves for the 300µm × 300µm sensor at different temperatures and for different dopant concentrations. The detection zone lies between the dotted lines in each plot.

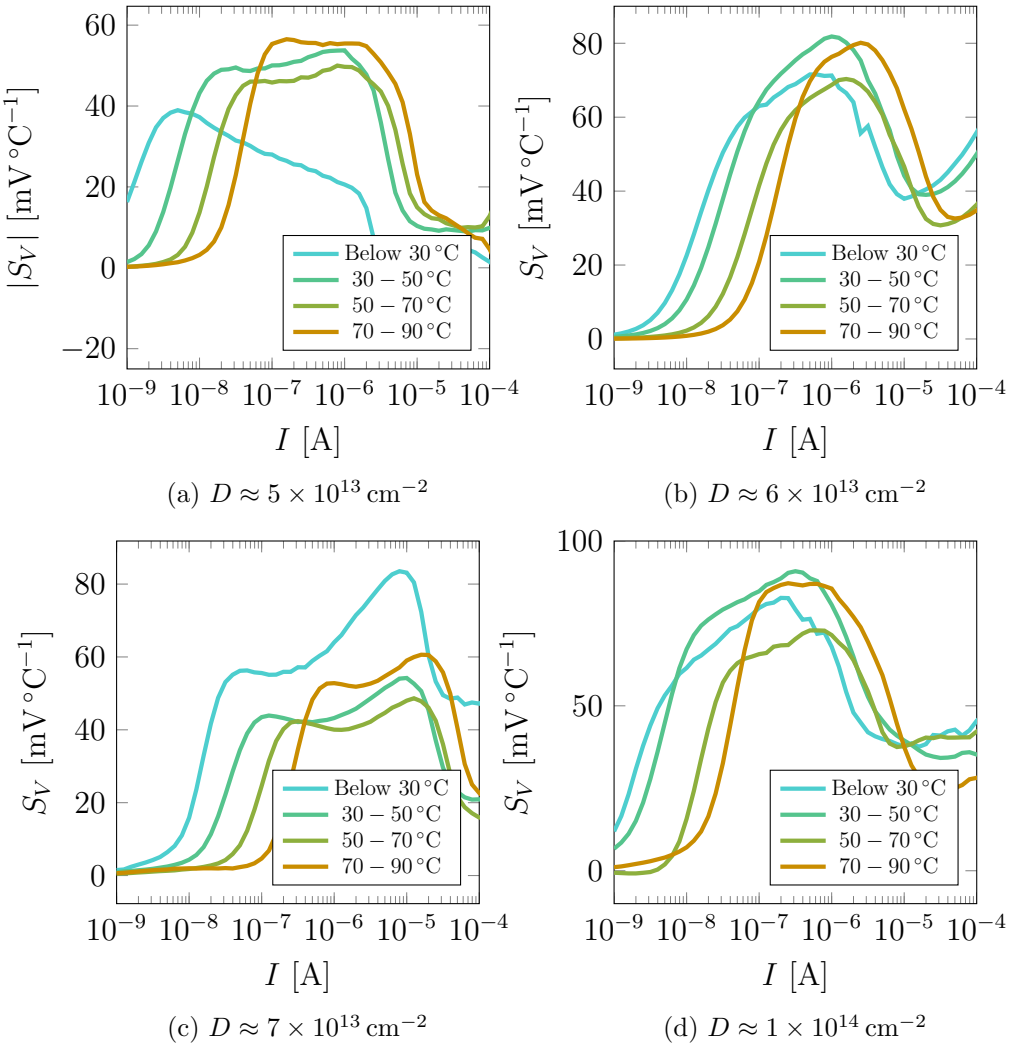

(a) $D \approx 5 \times 10^{13}\,\mathrm{cm}^{-2}$ (b) $D \approx 6 \times 10^{13}\,\mathrm{cm}^{-2}$

(c) $D \approx 7 \times 10^{13}\,\mathrm{cm}^{-2}$ (d) $D \approx 1 \times 10^{14}\,\mathrm{cm}^{-2}$

Figure B.19: Sensitivity curves for the 300µm × 300µm sensor at different temperatures and for different dopant concentrations.

Figure B.18, for $D \approx 7 \times 10^{13}\,\mathrm{cm}^{-3}$, the detection zone can reach 10 µA or more whereas for the other cases the current in the detection zone reaches a maximum of only a few micro-amperes.

Appendix C. Determining the wet-etching time

As mentioned earlier, the distinctive feature of the current iteration of these polysilicon sensors is the partial removal of the sacrificial layer underneath the PN−junctions to lower their thermal inertia. Hydrofluoric acid HF can attack the silicon oxide without damaging the silicon substrate. However, the etch rate of full strength HF is too fast to control during a process (typically $300\,\text{Å}\,\text{s}^{-1}$ at room temperature). For this reason, HF is usually mixed with water and ammonium fluoride NH_4F, which acts as a buffer to the generation of hydrogen ions that accelerate the etch. These solutions are called buffered oxide etches (BOE) and are mixed in different strengths to change the etch rate, which is also dependent on temperature ([22]). An increase in temperature of only a few degrees during the etch can lead to over-etching the silicon oxide layer, making the sensors more fragile. Prior to etching, the wafer undergoes a UV-ozone treatment to enhance the wetting characteristics of its surface which allows the BOE to easily penetrate the small openings (as in Figure 7b). The beaker containing the wafer and the solution are placed in an ultrasonic water tank. When the ultrasounds are turned on, the tank starts to heat up, slightly raising the temperature of the water. The temperature was monitored during the etch to make sure it does

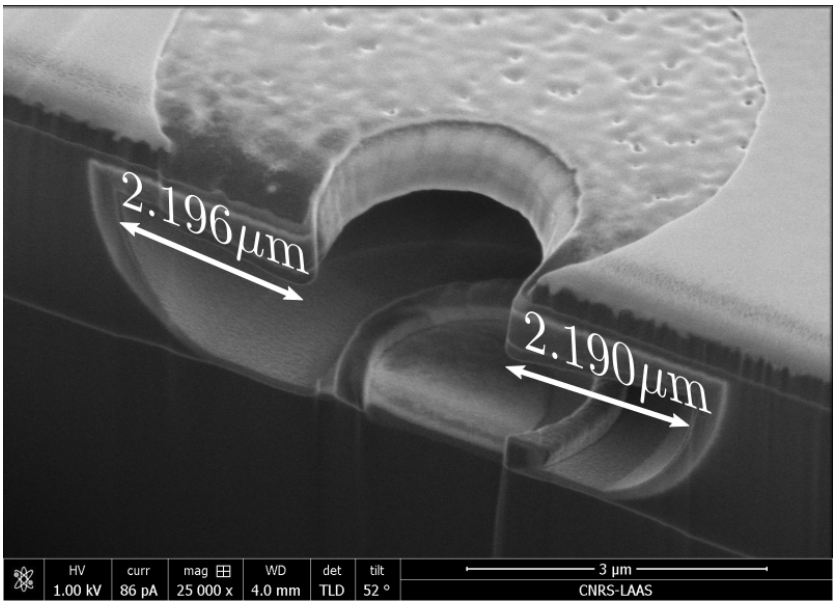

Figure C.20: SEM of partially suspended sensor

not exceed 28 °C.

The buffered-HF solution reaches the sacrificial SiO_x layer through holes in the polysilicon and silicon nitride layers opened in step 6 (section 2.2, Figures 6b) and in the passivation layer in step 10 (Figures 6e). Over-etching can occur in a matter of minutes, and can weaken the sensing area or cause it to break off of the polysilicon layer. In order to estimate the etching rate, one of the wafers is placed in the BOE for 20 min. The solution having a higher wetting on the silicon nitride layer covering the oxide than on the silicon surface underneath, the etching is quicker on the top side of the oxide layer as can be seen in Figure C.20. The etching rate is approximately $1100\,\text{Å}\,\text{min}^{-1}$. The annular shape in the etched region is likely silicon nitride residue from the RIE in step 10, but does not have an effect on the wet etch.

References

[1] H. F. Fabisch, Fluidics, in: J. J. McKetta Jr (Ed.), Encyclopedia of chemical processing and design, volume 23, Marcel Dekker Inc., 270 Madison Avenue, New York, New York, 10016, 1997, pp. 28–45.

[2] T. M. Weathers, NASA Contributions to Fluidic Systems, volume 10, 1973.

[3] R. Woszidlo, F. Ostermann, H. J. Schmidt, Fundamental properties of fluidic oscillators for flow control applications, AIAA Journal 57 (2019) 978–992.

[4] C. Nicholls, The analysis, modelling and acoustic control of fluidic devices, Ph.D. thesis, Oxford University, 2021.

[5] V. Tesař, Time-delay circuits for fluidic oscillators and pulse shapers, Energies 12 (2019).

[6] G. C. Saliba, A. Batikh, S. Colin, L. Baldas, Pulsed Impinging Jets for Heat Transfer: A Short Review, ASME Journal of Heat and Mass Transfer 145 (2023) 110801.

[7] S. Wang, A. Batikh, L. Baldas, A. Kourta, N. Mazellier, S. Colin, S. Orieux, On the modelling of the switching mechanisms of a Coanda fluidic oscillator, Sensors and Actuators, A: Physical 299 (2019) 1–12.

[8] G. C. Saliba, V. Raimbault, A. Batikh, S. Colin, L. Baldas, Relaxation Fluidic Oscillators: Design Parameters, New Operating Modes, and Characteristics of Their Internal and External Flows, Journal of Fluids Engineering 145 (2023) 101202.

[9] E. W. Simões, R. Furlan, R. E. Bruzetti Leminski, M. R. Gongora-Rubio, M. T. Pereira, N. I. Morimoto, J. J. Santiago Avilés, Microfluidic oscillator for gas flow control and measurement, Flow Measurement and Instrumentation 16 (2005) 7–12.

[10] J. T. Yang, C. K. Chen, I. C. Hu, P. C. Lyu, Design of a self-flapping microfluidic oscillator and diagnosis with fluorescence methods, Journal of Microelectromechanical Systems 16 (2007) 826–835.

[11] C. J. Chang, H. T. Chen, C. Gau, Flow and heat transfer of a microjet impinging on a heated chip: Part II - Heat transfer, Nanoscale and Microscale Thermophysical Engineering 17 (2013) 92–111.

[12] N. Kakuta, Y. Fukuhara, K. Kondo, H. Arimoto, Y. Yamada, Temperature imaging of water in a microchannel using thermal sensitivity of near-infrared absorption, Lab on a Chip 11 (2011) 3479–3486.

[13] T. Camps, J. Tasselli, J. Lubin, D. Lagrange, L. Bouscayrol, A. Marty, Development of polysilicon devices for microfluidic thermal instrumentation, Sensors and Actuators, A: Physical 189 (2013) 67–73.

[14] R. McAfee, M. Fish, J. Gess, Zener diode reverse breakdown voltage as a simultaneous heating and temperature sensing element, in: 2022 21st IEEE Intersociety Conference on Thermal and Thermomechanical Phenomena in Electronic Systems (iTherm), pp. 1–5.

[15] Y. Xia, G. M. Whitesides, Soft lithography, Angewandte Chemie - International Edition 37 (1998) 550–575.

[16] D. J. Hoelzle, B. A. Varghese, C. K. Chan, A. C. Rowat, A microfluidic technique to probe cell deformability, Journal of Visualized Experiments (2014) 7–9.

[17] H. R. Muller, A Study of the Dynamic Features of a Wall-Reattachment Fluid Amplifier, Journal of Basic Engineering 86 (1964) 819–826.

[18] U. Stöhr, P. Vulto, P. Hoppe, G. Urban, H. Reinecke, High-resolution permanent photoresist laminate for microsystem applications, Journal of Micro/Nanolithography, MEMS, and MOEMS 7 (2008) 033009.

[19] R. Courson, S. Cargou, V. Conédéra, M. Fouet, A. M. Gué, Low cost integration of multilevel lab-on-a-chip using a new generation of dry film photoresists, Smart Systems Integration - 8th International Conference and Exhibition on Integration Issues of Miniaturized Systems - MEMS, NEMS, ICs and Electronic Components, SSI 2014 (2014) 139–146.

[20] X. Huang, P. Li, Y. Tan, Analysis of time-dependent heat transfer of ellipsoidal protruded microchannel with multiple pulsating jets, Applied Thermal Engineering 210 (2022) 118348.

[21] Ö. Yalçın, G. Saliba, X. Gloerfelt, A. Batikh, L. Baldas, Numerical investigation of a pulsed jet actuator having non-negligible switching time, AIAA Journal (2023) 1–11.

[22] P. van Zant, Microchip Fabrication: A Practical Guide to Semiconductor Processing, McGrawhill, New York, 2014.